



Cite this: *CrystEngComm*, 2021, 23, 5531

# Slight ligand modifications within multitopic linear hydroxamates promotes connectivity differences in Cu(II) 1-D coordination polymers†

Mohammed B. Fugu,<sup>a</sup> Joe Coley,<sup>b</sup> Isabella F. Dickinson,<sup>a</sup> James B. Orton,<sup>c</sup> Wim Klooster,<sup>c</sup> M. Paul Gleeson<sup>d</sup> and Leigh F. Jones \*<sup>ab</sup>

The novel multitopic ligands *N*-hydroxy-4-((2-hydroxy-3-methoxybenzyl)amino)benzamide ( $L_3H_3$ ) and *N*-hydroxy-4-((2-hydroxybenzyl)amino)benzamide ( $L_4H_3$ ) have been synthesised through the Schiff base coupling and subsequent reduction of 4-aminophenylhydroxamic acid and either *o*-vanillin (to give  $L_3H_3$ ) or 2-hydroxybenzaldehyde (to give  $L_4H_3$ ). These linear multitopic ligands bind Cu(II) centres at both the hydroxamate and phenol ends to form the 1-D coordination polymers  $[Cu(II)(L_3H_2)_2]_n$  (**1**) and  $[Cu(II)(L_4H_2)_2 \cdot 2MeOH]_n$  (**2**). Slight differences in the structures of  $L_3H_3$  and  $L_4H_3$  lead to significant extended connectivity changes upon Cu(II) metalation that are exemplified by a 27% decrease in intra-chain Cu(II) ...Cu(II) distance upon moving from **1** to **2**. The significant conformation and metal binding differences shown by  $L_3H_2^-$  and  $L_4H_2^-$  in **1** and **2** respectively have been rationalised using density functional theory (DFT) calculations. Hirshfeld surface analysis has been employed to assess and visualise the intra- and intermolecular interactions in both complexes.

Received 18th June 2021,  
Accepted 22nd July 2021

DOI: 10.1039/d1ce00807b

rsc.li/crystengcomm

## Introduction

Coordination polymers (CPs) are extended network materials comprising repeating coordination entities that propagate along one (1-D), two (2-D) or three (3-D) directions and are derived from a combination of metal ion nodes and divergent bridging ligands.<sup>1</sup> Consequently, the resultant topology can often be tailored through careful node selection (metal ion geometry preferences)<sup>2</sup> and ligand design (number of functional sites and/or shape).<sup>3</sup> The ability to exercise synthetic and topological control over the assembly of a coordination polymer has enormous value to the synthetic chemist/materials scientist. Apart from the initial satisfaction it would derive, such undertakings give the protagonist more than a fighting chance of imparting the required functionality (or indeed multi-functionality) to

the resultant material.<sup>2,3</sup> Such applications may lie in one of a number of research fields that include molecular magnetism (such as spin-crossover behaviour (SCO));<sup>4</sup> single-chain magnets (SCM)<sup>5</sup> and single-ion magnetism (SIM)/single-molecule magnetism (SMM)<sup>6</sup>, electrical conductivity,<sup>7</sup> luminescence<sup>8,13c,e</sup> and homo-/heterogeneous catalysis.<sup>9,10a</sup> The latter relies on the designer transmitting porosity to their extended architectures.<sup>10</sup> Indeed, such porous materials are also of intense interest in areas such as gas storage and separation,<sup>11</sup> drug delivery<sup>12</sup> and sensor materials.<sup>4b,13</sup>

Previous work in our group has described the *in situ* formation (and Cu(II) ligation) of a series of ligands constructed from the Schiff base coupling of 2-amino-phenylhydroxamic acid and *o*-vanillin (and its analogues). The planarity of the resulting ligands (e.g. *o*-[(*E*)-(2-hydroxy-3-methoxyphenyl)methylideneamino]benzohydroxamic acid;  $L_1H_3$  in Scheme 1), gave rise to a family of layered planar Cu(II) cages ranging in nuclearity from  $[Cu(II)_{10}]$  to  $[Cu(II)_{30}]$ .<sup>14</sup> We went on to show that the selective one-pot imine reduction (using sodium triacetoxyborohydride)<sup>15</sup> of the *o*-[(*E*)-(2-hydroxy-3-methoxyphenyl)methylideneamino]benzohydroxamic acid ligand afforded the target ligand *N*-hydroxy-2-((2-hydroxy-3-methoxybenzyl)amino)benzamide ( $L_2H_3$ ; Scheme 1). The introduction of a secondary amine group rendered the resultant ligand non-planar as illustrated upon subsequent Cu(II) ligation when forming the 12-MC-4<sub>Cu(II)</sub> metallacrown  $[Cu(II)_5(L_2H_2)_4(MeOH)_2](NO_3)_2 \cdot 3H_2O \cdot 4MeOH$ .<sup>16</sup>

<sup>a</sup> School of Natural Sciences, Bangor University, Bangor, Wales, LL57 2DG, UK

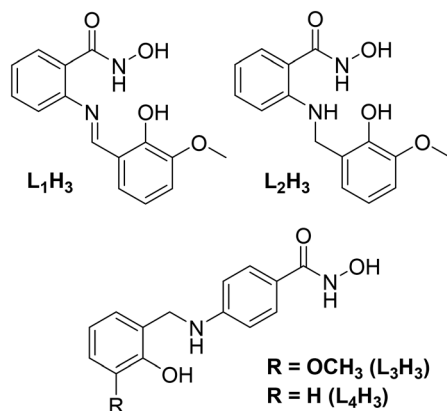
<sup>b</sup> School of Physical, Biological and Forensic Sciences, University of Wolverhampton, Wulfruna Street, Wolverhampton, England, WV1 1LY, UK. E-mail: Leigh.Jones@wlv.ac.uk; Tel: +44 (0)1902 32 1180

<sup>c</sup> UK National Crystallographic Service, Chemistry, Faculty of Natural and Environmental Sciences, University of Southampton, England, SO17 1BJ, UK

<sup>d</sup> School of Engineering, King Mongkut's Institute of Technology Ladkrabang, Bangkok 10520, Thailand

† Electronic supplementary information (ESI) available. CCDC 1941525 and 1941526. For ESI and crystallographic data in CIF or other electronic format see DOI: 10.1039/d1ce00807b





**Scheme 1** (Top) ChemDraw representation of the ligands *o*-[(*E*)-(2-hydroxy-3-methoxyphenyl)methylideneamino]benzohydroxamic acid (left;  $\text{L}_1\text{H}_3$ ) and *N*-hydroxy-2-((2-hydroxy-3-methoxybenzyl)amino)benzamide (right,  $\text{L}_2\text{H}_3$ ) previously used in the production of a series of polynuclear Cu(II) complexes (see main text for details). (Bottom) ChemDraw representation of the ligands *N*-hydroxy-4-((2-hydroxy-3-methoxybenzyl)amino)benzamide ( $\text{L}_3\text{H}_3$ ) and *N*-hydroxy-4-((2-hydroxybenzyl)amino)benzamide ( $\text{L}_4\text{H}_3$ ) used in this work.

## Results and discussion

In this work we describe the design, synthesis and Cu(II) ligation of the multitopic ligands *N*-hydroxy-4-((2-hydroxy-3-methoxybenzyl)amino)benzamide ( $\text{L}_3\text{H}_3$ ) and *N*-hydroxy-4-((2-hydroxybenzyl)amino)benzamide ( $\text{L}_4\text{H}_3$ ). Akin to ligands  $\text{L}_{1-2}\text{H}_3$  (Scheme 1), ligands  $\text{L}_3\text{H}_3$  and  $\text{L}_4\text{H}_3$  are forged through the Schiff base coupling and subsequent imine reduction of 4-amino-phenylhydroxamic acid and either *o*-vanillin ( $\text{L}_3\text{H}_3$ ) or salicylaldehyde ( $\text{L}_4\text{H}_3$ ) and differ only in the coupling site (the 2-position in  $\text{L}_{1-2}\text{H}_3$  *cf.* 4-position in  $\text{L}_{3-4}\text{H}_3$ ). The result is the formation of two linear multitopic ligands specifically designed to produce coordination polymers as demonstrated through the construction of the 1-D chains  $[\text{Cu}(\text{II})(\text{L}_3\text{H}_2)_2]_n$  (**1**) and  $\{[\text{Cu}(\text{II})(\text{L}_4\text{H}_2)_2] \cdot 2\text{MeOH}\}_n$  (**2**) as described below.

## Structural descriptions

$[\text{Cu}(\text{II})(\text{L}_3\text{H}_2)_2]_n$  (**1**) crystallises in the monoclinic  $P2_1/c$  space group and the asymmetric unit comprises one Cu(II) centre (Cu1) and one  $\text{L}_3\text{H}_2^-$  ligand. Each axially elongated J–T distorted octahedral Cu(II) centre in **1** is bound at the equatorial positions by two singly deprotonated  $\text{L}_3\text{H}_2^-$  ligands that chelate through their hydroxamate (O2) and carbonyl (O1) oxygen atoms (Cu1–O1 = 1.93 Å, Cu1–O2 = 1.91 Å). The axial sites at each metal centre are occupied through long contacts with  $\text{O}_{\text{phen}}$  oxygen atoms (O3 and s.e.) belonging to neighbouring  $\text{L}_3\text{H}_2^-$  ligands (Cu1–O3 = 2.74 Å and s.e.). Moreover, intra-ligand H-bonding interactions are observed between phenolic protons, H3H, and juxtaposed –OMe oxygen atoms (O4) (O3(H3H)⋯O4 = 2.16 Å). The multitopic nature of the  $\text{L}_3\text{H}_2^-$  moieties in **1** results in the formation of the ribbon topology chains in **1** as shown in Fig. 1. The individual chains in **1** propagate in superimposable rows along the *ac* plane of the unit cell and produce an intra-chain

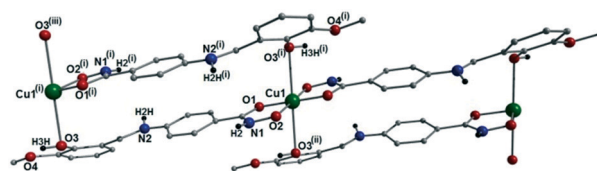


**Fig. 1** Crystal structure of the coordination polymer in  $[\text{Cu}(\text{II})(\text{L}_3\text{H}_2)_2]_n$  (**1**). Colour code as used throughout the text: green (Cu), grey (C), blue (N), red (O) and black (H). The majority of hydrogen atoms have been omitted for clarity. Symmetry codes: (i)  $1 + x, y, -1 + z$ ; (ii)  $-1 - x, 1 - y, 1 - z$  and (iii)  $2 + x, y, -2 + z$ .

Cu⋯Cu distance of 11.75 Å. The chains in **1** are stabilised by intra-chain  $\pi$ – $\pi$  interactions between neighbouring hydroxamate phenyl rings giving a  $[\text{C2}–\text{C6}]_{\text{centroid}} \cdots [\text{C2}'–\text{C6}']_{\text{centroid}}$  distance of 3.83 Å. The individual chains in **1** stack on top of one another in a superimposable manner and are connected through H-bonding interactions (*e.g.* N1(H2)⋯O2' = 2.03 Å, N2(H2H)⋯O2' = 2.38 Å and N2(H2H)⋯O3' = 2.95 Å) (Fig. 3). The resultant H-bonded stacks arrange themselves into the space efficient herring bone motif along the *b* direction of the unit cell and are also connected through a combination of H-bonding (C15(H15A)⋯O3' = 2.83 Å) and C–H⋯ $\pi$  interactions ( $[\text{C9}–14]_{\text{centroid}} \cdots (\text{H12}')\text{C12} = 3.10$  Å) (Fig. 2 and 3a).

Akin to **1**, the complex  $\{[\text{Cu}(\text{II})(\text{L}_4\text{H}_2)_2] \cdot 2\text{MeOH}\}_n$  (**2**) crystallises in the monoclinic  $P2_1/c$  space group (Table 2). The asymmetric unit comprises an axially elongated Cu(II) centre, a single  $\text{L}_4\text{H}_2^-$  ligand and a methanol solvent of

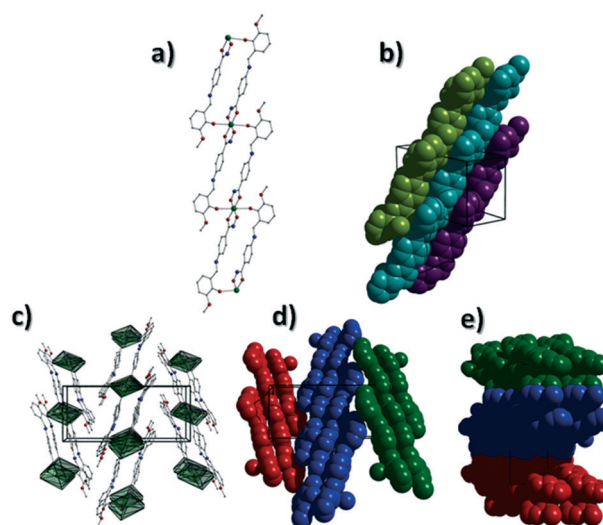


**Fig. 2** (a) A polyhedral representation of a single chain in **1** highlighting the ribbon topology. All hydrogen atoms have been omitted for clarity. (b) Space-fill represented and colour coded H-bonded stacks of chains in **1** as viewed along the *ab* plane of the unit cell. Each colour represents a single chain. (c) Polyhedral representation of the packing observed in **1**. (d and e) Space-fill and colour coded representation of H-bonded stacks comprising multiple 1D chains of **1** as viewed along the *a* (d) and *c* (e) unit cell direction. Note: figures c and d are equivalent and represent polyhedral (c) and space-fill (d) forms, respectively.



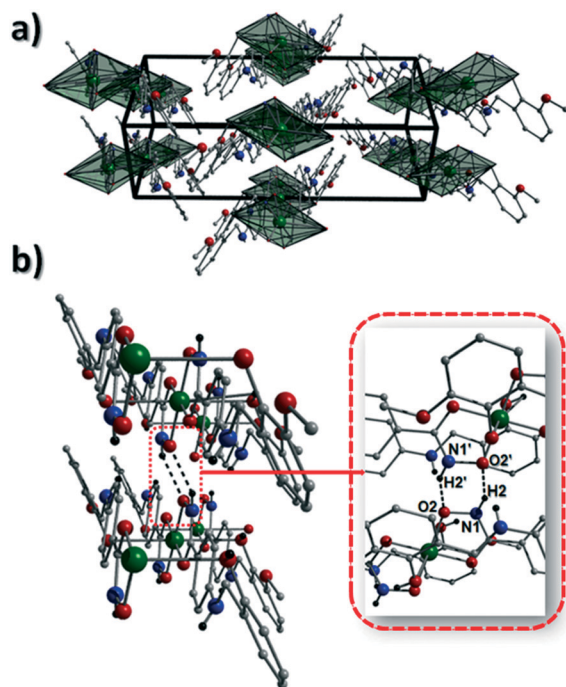


**Fig. 3** (a) Packing in **1** highlighting the individual 1-D chains stacking along the *ac* unit cell direction. (b) Two individual  $\{\text{Cu(II)}(\text{L}_3\text{H}_2)_2\}$  chains connected through inter-chain complementary hydrogen bonding represented as dashed lines ( $\text{N1(H2)}\cdots\text{O2}' = 2.03 \text{ \AA}$ ).

crystallisation that sits at a H-bonding distance from the amide proton of the hydroxamate section of the ligand ( $\text{N1(H1N)}\cdots\text{O4} = 1.98 \text{ \AA}$ ; Fig. 4a). Two  $\text{L}_4\text{H}_2^-$  ligands chelate to the metal centre at distances of  $1.91 \text{ \AA}$  ( $\text{Cu1-O1}$ ) and  $1.93 \text{ \AA}$  ( $\text{Cu1-O2}$ ) to give the  $\{\text{Cu(II)}(\text{L}_4\text{H}_2)_2\}$  chair shaped building block in **2** as opposed to the near planar  $\{\text{Cu(II)}(\text{L}_3\text{H}_2)_2\}$  units in **1** (Fig. 4a *cf.* 1). The major difference between the structure in **1** *cf.* **2** lies in the axial connectivity at the  $\text{Cu(II)}$  centres in **2**. Here, the 1-D chains in **2** are propagated by extremely long axial contacts between the metal centres and secondary amine N atoms ( $\text{N2}$ ) located at the junction of the hydroxamate and phenolic units within each  $\text{L}_4\text{H}_2^-$  ligand ( $\text{Cu1-N2}' = 3.04 \text{ \AA}$ ), as opposed to the  $\text{O}_{\text{phen}}$  oxygen donor atoms in **1** (Fig. 1 *cf.* 4b). Indeed, a  $\text{Cu(II)}-\text{N}$  distance of  $3.04 \text{ \AA}$  is greater than the sum of their van der Waals radii ( $\sim 2.95 \text{ \AA}$ ) and this interaction should be deemed weak, as corroborated using Hirshfeld surface analysis (*vide infra*).

The result is a much shorter intra-chain  $\text{Cu1}\cdots\text{Cu1}'$  distance of  $8.62 \text{ \AA}$  in **2** (*cf.*  $11.75 \text{ \AA}$  in **1**) (Fig. 4b). More specifically, this ligand modification gives rise to a 27% decrease in the intra-nodal ( $\text{Cu(II)}\cdots\text{Cu(II)}$ ) distance on moving from **1** to **2**. Interestingly, the deliberate omission of the  $-\text{OMe}$  group in  $\text{L}_4\text{H}_3$  allows each ligand to distort to a much greater extent than observed in **1** (Fig. 5). More specifically, the phenolic aromatic rings in **2** twist away from their phenyl hydroxamate counterparts to produce a torsion angle of  $75.1^\circ$  ( $\text{C5-N2-C8-C9}$ ) compared to the more coplanar value of  $164.5^\circ$  ( $\text{C5-N2-C8-C9}$ ) exhibited by the  $\text{L}_3\text{H}_2^-$  units in **1** (Fig. 5a *cf.* c). These distortions can also be

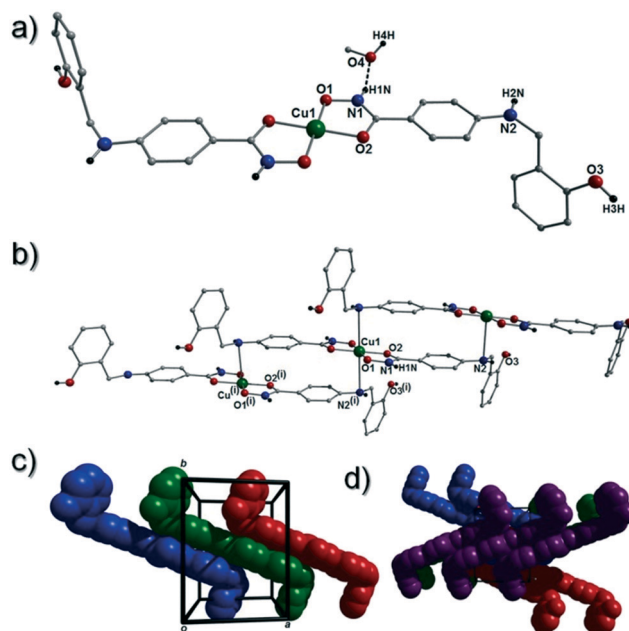


**Fig. 4** (a) A single  $\{[\text{Cu(II)}(\text{L}_4\text{H}_2)_2]\cdot 2\text{MeOH}\}$  unit in **2**. The asymmetric unit has been labelled and only one MeOH solvent of crystallisation is shown. The dashes black line shows an inter-molecular H-bond at a distance of  $1.98 \text{ \AA}$  ( $\text{N1(H1N)}\cdots\text{O4}$ ). The chain arrangement in **2** as viewed in normal (b) and space-fill mode (c), where each colour represents an independent  $\{\text{Cu(II)}(\text{L}_4\text{H}_2)_2\}$  unit (symmetry code: (i) =  $1 + x, y, z$ ). (d) Space-fill representation of the packing in **2**. Each colour represents an H-bonded stack of 1-D chains in **2** as viewed along the *c* unit cell direction.

quantified by assessing the dihedral angles forged between the two aromatic rings belonging to each ligand ( $35.8^\circ$  in **1** and  $84.6^\circ$  in **2**) (Fig. 5). Computational studies have been carried in an attempt to rationalise these differences and are

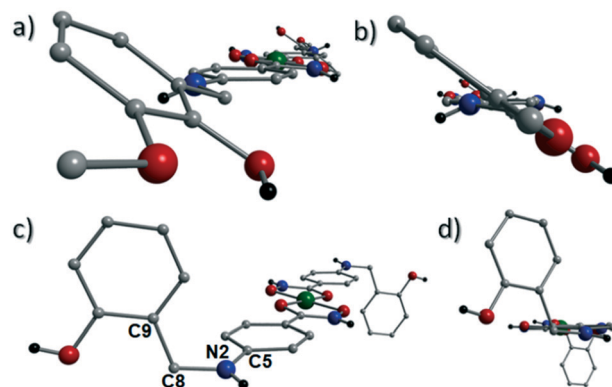


**Fig. 5** The coordination polymers in **1** (a and b) and **2** (c and d) highlighting significant differences in phenolic ring positions in relation to their conjoined hydroxamate fragments. The planes of the phenolic and hydroxamate aromatic rings in **1** lie at an angle of  $35.8^\circ$  from one another as illustrated in figure b (the equivalent dihedral angle in **2** is  $84.6^\circ$ ; fig. c). Figure c also highlights the  $\text{C5-N2-C8-C9}$  torsion angle of  $164.5^\circ$  in **2**. The equivalent torsion in **1** (also labelled  $\text{C5-N2-C8-C9}$ ) provides an angle of  $75.1^\circ$  (a).





described later in this work. The individual chains in **2** propagate in a step-like manner along the *a* direction of the unit cell (Fig. 4b) and arrange themselves in space efficient stacks along the *ab* plane. These individual stacks pack along the *c*-direction in an alternating fashion, as highlighted in Fig. 4d. The methanol solvents of crystallisation (labelled C15–O4(H4H)) sit at H-bonding distance from  $L_4H_2^-$  amide N atoms at a distance of 1.98 Å ( $N1(H1N) \cdots O4$ ) and act as molecular mortar by forming an O–H $\cdots\pi$  interactions with both nearby phenolic rings ( $O4(H4H) \cdots [C9-C14]_{\text{centroid}} = 2.54$  Å) and  $O_{\text{phen}}$  oxygen donor atoms ( $O3$ ) ( $O3 \cdots (H15C')C15' = 2.67$  Å). The  $L_3H_2^-$  secondary amine N atoms ( $N2$  and s.e.) also partake in inter-chain H-bonding with neighbouring ligand  $O_{\text{phen}}$  aromatic rings ( $N2(H2N) \cdots [C9'-C14']_{\text{centroid}} = 3.14$  Å). The IR spectra of  $[Cu(II)(L_3H_2)_2]_n$  (**1**) and  $\{[Cu(II)(L_4H_2)_2] \cdot 2MeOH\}_n$  (**2**) show bands centred around 1608–1588  $\text{cm}^{-1}$  in **1** and 1606–1592  $\text{cm}^{-1}$  in **2** and are attributed to the ketonic C=O stretching modes associated with the hydroxamate  $L_3H_2^-$  and  $L_4H_2^-$  ligands, while resonances at 1064  $\text{cm}^{-1}$  in **1** and 1079  $\text{cm}^{-1}$  in **2** are assigned to N–O stretches and in combination corroborate the chelating nature of these hydroxamate ligands. Peaks at 1439  $\text{cm}^{-1}$  and 1452  $\text{cm}^{-1}$  in **1** and 1414  $\text{cm}^{-1}$  and 1453  $\text{cm}^{-1}$  in **2** are attributed to N–H deformation and C–N stretching frequencies, respectively.<sup>17</sup>

### Hirshfeld surface studies

The close intermolecular interactions in **1** and **2** were further surveyed and visualised by carrying out a Hirshfeld surface (HS) analysis using the  $d_{\text{norm}}$ , curvedness and shape index mapping functions.<sup>18</sup> Fig. 6 and 8 depict the Hirshfeld surfaces (mapped over  $d_{\text{norm}}$ ) for  $[Cu(II)(L_3H_2)_2]_n$  (**1**) and

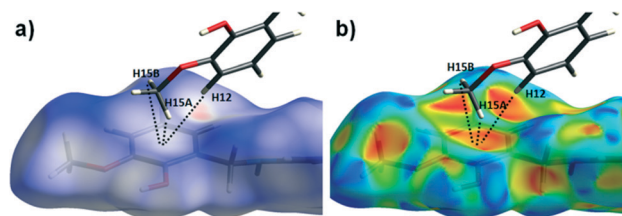


Fig. 7 The  $d_{\text{norm}}$  (a) and shape index (b) Hirshfeld surfaces for **1**, highlighting the inter-chain C–H $\cdots\pi$  interactions:  $C12(H12) \cdots [C9'-C14']_{\text{centroid}} = 3.10$  Å;  $C15(H15A) \cdots [C9'-C14']_{\text{centroid}} = 3.53$  Å and  $C12(H15B) \cdots [C9'-C14']_{\text{centroid}} = 3.48$  Å (these are distances taken from the crystal structure data).

$\{[Cu(II)(L_4H_2)_2] \cdot 2MeOH\}_n$  (**2**), respectively. In these plots, the red, blue and white regions represent interatomic interactions that are shorter (red), longer (blue) and commensurate (white) with vdW separations. Therefore, a close intermolecular interaction is envisaged when a particular vicinity of a molecules surface exhibits a red region of colouration. This is illustrated in Fig. 6 as it shows (for instance): 1) an inter-chain C–H $\cdots\pi$  interaction at a distance of 2.7 Å (corresponding to the  $C8(H8A) \cdots O1' = 2.8$  Å interaction observed in the crystal structure (Fig. 6a and b)) and 2) inter-chain complementary H-bonds between two adjacent hydroxamate functional groups at a distance of 1.88 Å (corresponding to the  $N1(H2) \cdots O2' = 2.03$  Å interaction observed in the crystal structure) (Fig. 6d). The Cu1–O3' long axial contact that allows chain propagation in **1** is also observed here at a distance of 2.74 Å (Fig. 6b and c). The inter-chain C–H $\cdots\pi$  interactions in **1** can be observed in the  $d_{\text{norm}}$  and shape index Hirshfeld surfaces given in Fig. 7. Likewise, the inter-chain C–H $\cdots\pi$  interactions observed in **2** ( $C11(H11) \cdots [C2'-C7']_{\text{centroid}} = 3.44$  Å and s.e.) are also corroborated using  $d_{\text{norm}}$  and shape index HS analysis (Fig. S10†).

The Hirshfeld surface ( $d_{\text{norm}}$ ) of  $\{[Cu(II)(L_4H_2)_2] \cdot 2MeOH\}_n$  (**2**) shows a number of intermolecular H-bonding interactions in the crystal. For instance, a short contact between  $O_{\text{phen}}$

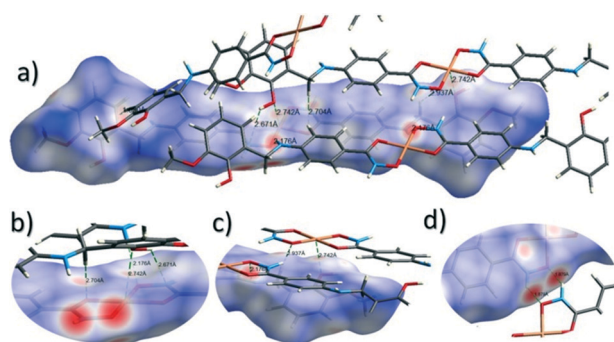


Fig. 6 Hirshfeld surface analysis of  $[Cu(II)(L_3H_2)_2]_n$  (**1**) mapped over the  $d_{\text{norm}}$  function (–0.56 to +1.37 a.u.<sup>–1</sup>) highlighting a number of intermolecular interactions observed in the crystal structure including the Cu–O3' long contact at a distance of 2.74 Å (figures a–c). Figure d shows complementary hydrogen bonding between juxtaposed hydroxamate functional groups at a distance of 1.88 Å ( $N1(H2) \cdots O2'$ ). Note: the CrystalExplorer program normalises all X–H bond lengths to values obtained experimentally from neutron diffraction studies. The red and blue spots highlight long and short interatomic contacts, respectively. White regions represent interatomic distances commensurate with van der Waals separations.

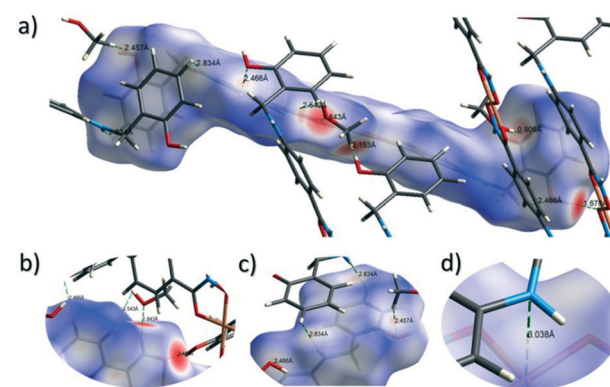


Fig. 8 Hirshfeld surface analysis of  $\{[Cu(II)(L_4H_2)_2] \cdot 2MeOH\}_n$  (**2**) using the  $d_{\text{norm}}$  function (–0.73 to +1.45 a.u.<sup>–1</sup>) and highlighting a number of inter-molecular interactions (a–c) including the very weak Cu1–N2' = 3.04 Å long contact (d).



protons (H3H and s.e.) and juxtaposed hydroxamate O donor atoms (O1 and s.e.) is highlighted in Fig. 8a, giving a distance of 1.68 Å. This interaction corresponds to the O3(H3H)⋯O1' = 1.81 Å interaction observed in the crystal structure of **2**. A significant H-bonding interaction is also observed (1.84 Å) between the MeOH solvent of crystallisation and a neighbouring hydroxamate N-H group and correlates with the N1(H1N)⋯O4 = 1.98 Å interaction observed in the crystal structure (Fig. 8b). As predicted, the HS plot centred on the Cu1–N2' interaction in **2** is indeed indicative of a weak interaction (white colouration), with a distance at the very limit of the sum of their individual van der Waals radii (3.04 Å; Fig. 8d). The intermolecular interactions in **1** and **2** can also be visualised through their Hirshfeld surfaces mapped over both curvedness (Fig. S6 and S8†) and shape index (Fig. S7 and S9†). The curvedness plots in **1** and **2** each indicate flat regions around their aromatic rings (as expected), while the shape index surfaces for both complexes visualise the 'bumps and hollows' (shown as blue and red spots, respectively) associated with intermolecular interactions first highlighted *via* their  $d_{\text{norm}}$  surface plots in Fig. 6 and 8.

Contributions to the surface of the molecule from each atom in [Cu(II)(L<sub>3</sub>H<sub>2</sub>)<sub>2</sub>]<sub>n</sub> (**1**) and {[Cu(II)(L<sub>4</sub>H<sub>2</sub>)<sub>2</sub>·2MeOH]<sub>n</sub> (**2**) shows that the majority of their intermolecular interactions come from H⋯H contacts (41.6% (**1**) and 46.4% (**2**)) (Table 1).<sup>19</sup> Other significant contributions to the overall surface come from reciprocated C⋯H (26.2% in **1** and 21.3% in **2**) and O⋯H (20.4% in **1** and 21.8% in **2**) interactions. As is commonly observed, much smaller contributions are provided by N⋯H/H⋯N hydrogen bonding interactions (2.9% in **1** and 1.5% in **2**). The Cu–O and Cu–N long contacts that effectively allow chain propagation in **1** and **2** provide 1.7% and 1.0% contributions to their molecular surfaces as shown in the 2-D fingerprint plots of Fig. 9f (**1**) and 10f (**2**), respectively.

**Table 1** Relative percentage of close contact interactions contributing to the Hirshfeld surfaces in **1** and **2**. For a full breakdown analysis see Tables S2 and S3†

[Cu(II)(L <sub>3</sub> H <sub>2</sub> ) <sub>2</sub> ] <sub>n</sub> ( <b>1</b> )	
Contact	Percentage contribution (%)
H⋯H	41.6
C⋯H/H⋯C	26.2
O⋯H/H⋯O	20.4
N⋯H/H⋯N	2.9
C⋯C	2.9
Cu⋯O/O⋯Cu	1.7
O⋯O	1.3
N⋯C/C⋯N	0.4
{[Cu(II)(L <sub>4</sub> H <sub>2</sub> ) <sub>2</sub> ·2MeOH] <sub>n</sub> ( <b>2</b> )	
H⋯H	46.4
O⋯H/H⋯O	21.8
C⋯H/H⋯C	21.3
C⋯C	3.0
N⋯H/H⋯N	1.5
Cu⋯N/N⋯Cu	1.0
N⋯C/C⋯N	0.9
N⋯O/O⋯N	0.2

**Table 2** Selected crystal data obtained from **1** and **2**

	<b>1</b>	<b>2</b> ·2MeOH
Formula <sup>a</sup>	C <sub>30</sub> H <sub>30</sub> N <sub>4</sub> O <sub>8</sub> Cu <sub>1</sub>	C <sub>30</sub> H <sub>34</sub> N <sub>4</sub> O <sub>8</sub> Cu <sub>1</sub>
<i>M</i> <sub>w</sub>	638.12	642.15
Crystal system	Monoclinic	Monoclinic
Space group	<i>P</i> 2 <sub>1</sub> / <i>c</i>	<i>P</i> 2 <sub>1</sub> / <i>c</i>
<i>a</i> /Å	6.7098(2)	8.61560(10)
<i>b</i> /Å	21.4689(8)	11.31420(10)
<i>c</i> /Å	9.4280(2)	14.8436(2)
<i>α</i> /°	90	90
<i>β</i> /°	91.889(2)	100.8870(10)
<i>γ</i> /°	90	90
<i>V</i> /Å <sup>3</sup>	1357.38(7)	1420.89(3)
<i>Z</i>	2	2
<i>T</i> /K	100.0(2)	100.0(2)
<i>λ</i> <sup>b</sup> /Å	0.71073	0.71073
<i>D</i> <sub>c</sub> /g cm <sup>−3</sup>	1.561	1.501
<i>μ</i> (Mo–Kα)/mm <sup>−1</sup>	0.867	0.828
Meas./indep. ( <i>R</i> <sub>int</sub> ) refl.	26 867/9697 (0.0487)	12 946/11 113 (0.0206)
Restraints, parameters	0, 205	0, 199
<i>wR</i> <sub>2</sub> (all data) <sup>c</sup>	0.1113	0.1406
<i>R</i> <sub>1</sub> <sup>d,e</sup>	0.0481	0.0424
Goodness of fit on <i>F</i> <sup>2</sup>	1.303	1.138

<sup>a</sup> Includes guest molecules. <sup>b</sup> Mo–Kα radiation, graphite monochromator. <sup>c</sup>  $wR_2 = [\sum w(|F_o|^2 - |F_c|^2)|^2 / \sum w|F_o|^2]^{1/2}$ . <sup>d</sup> For observed data. <sup>e</sup>  $R_1 = \sum ||F_o| - |F_c|| / \sum |F_o|$ .

## Geometry optimisation studies

The more extreme distortion observed by the L<sub>4</sub>H<sub>2</sub><sup>−</sup> units in **2** when compared to the L<sub>3</sub>H<sub>2</sub><sup>−</sup> in **1** also give rise to differing Cu(II) binding sites at the phenolic sections of the ligands. We found it interesting that a metal binding site change is imposed through the omission of just one –OMe group. In order to gain insights into these observations, theoretical models of the two distinct geometries were created and geometry optimization computational studies were conducted using a cluster model derived from the two X-ray structures. Models of [Cu(II)(L)<sub>2</sub>] in the two configuration observed were fully optimized as described previously. The fundamental difference in the two conformations is the relative orientation

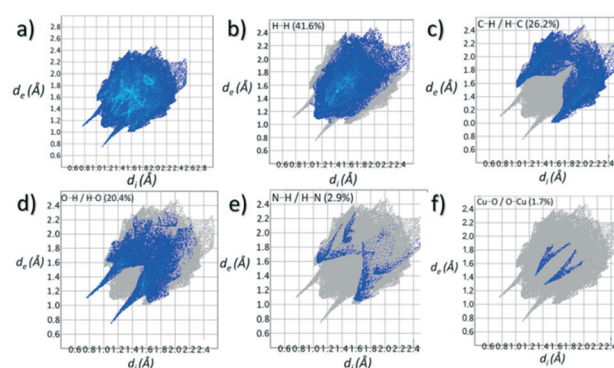


**Fig. 9** (a) Full 2-D fingerprint surface interactions plot for [Cu(II)(L<sub>3</sub>H<sub>2</sub>)<sub>2</sub>]<sub>n</sub> (**1**) along with plots for H⋯H (b), C⋯H/H⋯C (c), O⋯H/H⋯O (d), N⋯H/H⋯N (e) and Cu⋯O/O⋯Cu (f) contacts (*d*<sub>i</sub> = internal distance, *d*<sub>e</sub> = external distance in Å).



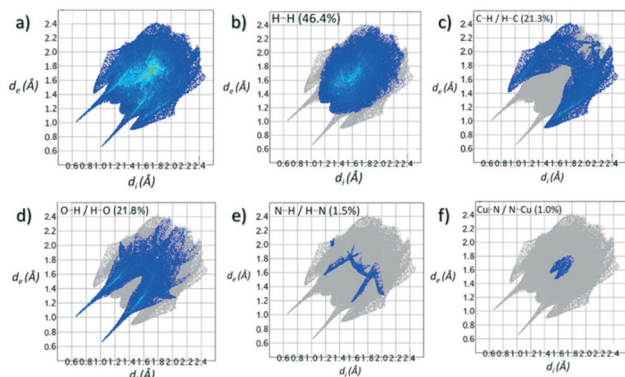


**Fig. 10** (a) Full 2-D fingerprint surface interactions plot for  $[\text{Cu}(\text{II})(\text{L}_4\text{H}_2)_2] \cdot 2\text{MeOH}$  (2) along with plots for  $\text{H} \cdots \text{H}$  (b),  $\text{C} \cdots \text{H}/\text{H} \cdots \text{C}$  (c),  $\text{O} \cdots \text{H}/\text{H} \cdots \text{O}$  (d),  $\text{N} \cdots \text{H}/\text{H} \cdots \text{N}$  (e) and  $\text{Cu} \cdots \text{N}/\text{N} \cdots \text{Cu}$  (f) contacts ( $d_i$  = internal distance,  $d_e$  = external distance in Å).

of the two ligand phenyl rings as indicated in Fig. 11. In  $\text{L}_3\text{H}_2^-$ , the rings are found to exist in the same plane ( $\sim 180^\circ$ ) while for  $\text{L}_4\text{H}_2^-$ , they adopt a conformation orthogonal ( $\sim 90^\circ$ ) to each other. The calculations showed that the *orthogonal* conformation was energetically preferred for both ligands in 1 and 2. While this conformation is indeed observed in the experimental crystal structure of 2, the planar configuration is found for 1. Further analysis showed that the energy penalty for 2 to adopt the less preferential conformation is just  $1.2 \text{ kcal mol}^{-1}$ , whereas it is considerably larger for 1, at  $3.5 \text{ kcal mol}^{-1}$ . It would therefore appear that the conformation observed in 2 is a function of the lower energy penalty associated with the orthogonal geometry, while complex 1 (exhibiting a more planar geometry) gains additional stabilization from the axial  $\text{Cu}-\text{O}_{\text{phen}}$  interactions (strong electron donor ROH groups) observed with adjacent ligands in the crystal lattice, leading to the 1-D chain topology.

Powder X-ray diffraction studies on 1 and 2 were used to confirm that their bulk samples were consistent with their

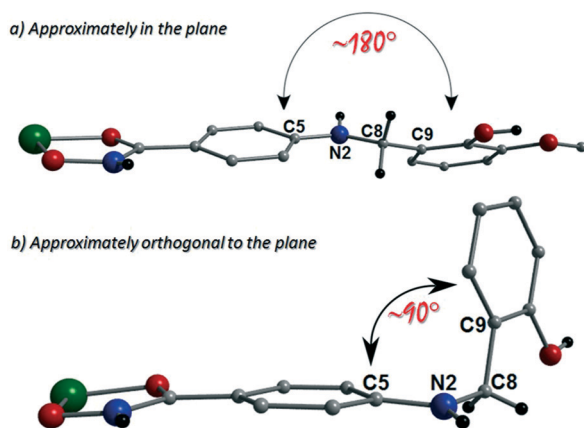


**Fig. 11** Schematic using crystal data from  $[\text{Cu}(\text{II})(\text{L}_3\text{H}_2)_2]$  (1) (a) and  $[\text{Cu}(\text{II})(\text{L}_4\text{H}_2)_2] \cdot 2\text{MeOH}$  (2) (b) to highlight the approximately *planar* and *orthogonal* positions in relation to their respected ligand aromatic rings.

single crystal data (Fig. S2 and S3†). This was carried out using simulations produced by the Mercury software package.<sup>20</sup> Using a Johnson Matthey balance, the room temperature magnetic moment ( $\mu_{\text{eff}}$ ) of 1 (1.69 BM) and 2 (1.64 BM) was found to be consistent with that expected for a magnetically dilute  $\text{Cu}(\text{II})$  chain ( $\mu_{\text{s.o.}} = 1.73 \text{ BM}$ ) (Table S1†).†

## Conclusions

We have described in this work the design and synthesis of the novel linear multitopic ligands *N*-hydroxy-4-((2-hydroxy-3-methoxybenzyl)amino)benzamide ( $\text{L}_3\text{H}_3$ ) and *N*-hydroxy-4-((2-hydroxybenzyl)amino)benzamide ( $\text{L}_4\text{H}_3$ ). Upon  $\text{Cu}(\text{II})$  ligation the self-assembly of the 1-D chains  $[\text{Cu}(\text{II})(\text{L}_3\text{H}_2)_2]_n$  (1) and  $[\text{Cu}(\text{II})(\text{L}_4\text{H}_2)_2] \cdot 2\text{MeOH}$  (2) is observed. Slight differences in the functionality of ligands  $\text{L}_3\text{H}_3$  vs.  $\text{L}_4\text{H}_3$ , namely the omission of an  $-\text{OMe}$  group in the latter, give rise to pertinent connectivity changes when closely inspecting chains 1 and 2. This is best exemplified by noting that the intra-nodal  $\text{Cu}(\text{II}) \cdots \text{Cu}(\text{II})$  distance in 2 is significantly shorter than the corresponding length in 1 ( $11.75 \text{ Å}$  (1) cf.  $8.62 \text{ Å}$  (2)). Although both these distances are too long for the possibility of magnetic exchange, such observations highlight the importance of ligand design and the potential ramifications associated with even slight modifications when designing magnetic coordination polymers. The coordination number and geometry flexibility of the  $\text{Cu}(\text{II})$  ion no doubt promotes successful CP formation in this work. Indeed, this is highlighted further when we note that attempts to produce other 1st row transition metal analogues have so far been fruitless. Nevertheless, work is ongoing on the elucidation of viable synthetic pathways for further metal coordination of the novel ligands  $\text{L}_3\text{H}_3$  and  $\text{L}_4\text{H}_3$ . Hirshfeld surface studies on both  $[\text{Cu}(\text{II})(\text{L}_3\text{H}_2)_2]_n$  (1) and  $[\text{Cu}(\text{II})(\text{L}_4\text{H}_2)_2] \cdot 2\text{MeOH}$  (2) have been employed to map and visualise all intermolecular interactions and to this end showed good alignment with contacts previously proposed upon close inspection of their crystal structures. Geometry optimisation computational studies were carried out on both complexes in order to probe the experimentally observed differences in their ligand conformations. It was shown that the  $\sim 90^\circ$  *orthogonal* geometry (with respect to the dihedral angle produces by their ligand aromatic rings), was preferred in both cases, although the observation was more pronounced in 2 over 1.

## Experimental section

### Materials

All solvent and chemicals were used as purchased. All chemicals were purchased from Sigma Aldrich.

† The powder spectrum obtained from  $[\text{Cu}(\text{II})(\text{L}_4\text{H}_2)_2] \cdot 2\text{MeOH}$  (2) shows signs of crystallinity loss (peak broadening) presumably during sample preparation (e.g. loss of interstitial MeOH solvent molecules of crystallisation upon exposure to air and sample grinding).





## Analytical methods

Infra-red spectra were recorded on a Perkin Elmer FT-IR Spectrum 100 spectrometer (School of Natural Sciences, Bangor University).  $^1\text{H}$  and  $^{13}\text{C}$  NMR spectra were obtained at room temperature (298 K) on a Bruker Ultrashield™ 400 Plus with Sample Xpress at 400 MHz. Chemical shifts are reported in ppm and referenced to DMSO ( $^1\text{H}$ : 2.50 ppm,  $^{13}\text{C}$ : 39.52 ppm). Elemental analysis was carried out at OEA Laboratories (Kelly Bray, Cornwall). The room temperature magnetic moments ( $\mu_{\text{eff}}$ ) for **1** and **2** were obtained using a Johnson Matthey balance situated at the School of Natural Sciences, Bangor University (see ESI† for more details).

## X-ray crystallography

Complexes **1** and **2** were collected on an Rigaku AFC12 goniometer equipped with an enhanced sensitivity (HG) Saturn724+ detector mounted at the window of an FR-E+ Super Bright molybdenum rotating anode generator with HF Varimax optics (100 m focus) (CCDC numbers: 1941525 (**1**) and 1941526 (**2**)). The cell determination and data collection of each complex was carried out using the CrystalClear-SM Expert package (Rigaku, 2012). Each data reduction, cell refinement and absorption correction were carried out using CrysAlisPro software (Rigaku OD, 2015),<sup>21</sup> while all structures were solved and refined using SHELXT and SHELXL-2014 (ref. 22) within OLEX-2.<sup>23</sup> Powder XRD was carried out using a PANalytical Philips X'Pert 3040/60 diffractometer at 45 kV and 35 mA between 5 and 60°  $2\theta$  using Ni-filtered Cu-K $\alpha_1$  radiation ( $\lambda = 1.5405 \text{ \AA}$ ) at the School of Natural Sciences, Bangor University.

## Computational methodology

Computational models of complexes **1** and **2** were constructed from their experimental X-ray coordinates. Both models comprise of a Cu(II) metal centre coordinated to two linear hydroxamate ligands  $[\text{Cu}(\text{II})(\text{L}_{3-4}\text{H}_2)_2]$ . The complexes were fully optimized in Gaussian G16 (ref. 24) using the DFT M062x functional<sup>25</sup> and the 6-311+G(d,p) basis set for H, N, C, O atoms and TZVP for Cu. Geometry optimizations were performed using default settings. Two additional models were generated by modifying the model of  $\text{L}_3\text{H}_2^-$  into  $\text{L}_4\text{H}_2^-$ , and *vice versa*. The relative energies associated with each configuration were then determined for both ligands. Hirshfeld surface analysis was carried out using the CrystalExplorer software.<sup>26</sup>

## Preparation of ligands $\text{L}_3\text{H}_3$ and $\text{L}_4\text{H}_3$

The synthesis of ligands *N*-hydroxy-4-((2-hydroxy-3-methoxybenzyl)amino)benzamide ( $\text{L}_3\text{H}_3$ ) and *N*-hydroxy-4-((2-hydroxybenzyl)amino)benzamide ( $\text{L}_4\text{H}_3$ ) along with their precursors are described in the ESI.†

## Preparation of complexes **1** and **2**

All reactions were performed under aerobic conditions and all reagents and solvents were used as purchased. **Caution:** although no problems were encountered in this work, care should be taken when manipulating the potentially explosive nitrate salts.

## Synthesis of $[\text{Cu}(\text{II})(\text{L}_3\text{H}_2)_2]_n$ (**1**)

$\text{Cu}(\text{NO}_3)_2 \cdot 3\text{H}_2\text{O}$  (0.025 g, 0.10 mmol), 4-((2-hydroxy-3-methoxybenzyl)amino)-*N*-hydroxybenzamide ( $\text{L}_3\text{H}_3$ ) (0.030 g, 0.10 mmol) and tetraethylammonium hydroxide (TEAOH) (0.015 g, 0.10 mmol) were dissolved in methanol (20 cm<sup>3</sup>) and the resultant solution stirred for 3 h at room temperature. The resultant yellow-green solution was then filtered and X-ray quality crystals of **1** were obtained upon slow evaporation of the mother liquor in 18% (11.5 mg; crystals) yield. Elemental analysis (%) calculated as  $\text{1} \cdot \text{H}_2\text{O}$  ( $\text{C}_{30}\text{H}_{32}\text{N}_4\text{O}_9\text{Cu}_1$ ): C 54.92, H 4.92, N 8.54; found: C 54.25, H 4.83, N 8.76. FT-IR (cm<sup>-1</sup>): 3498 (m), 3313 (w), 3189 (w), 2955 (w), 2837 (w), 1608 (s, sh), 1588 (s), 1562 (m), 1543 (w), 1477 (s), 1452 (m), 1439 (m), 1393 (w), 1358 (m), 1335 (w), 1271 (m), 1257 (w), 1211 (m), 1188 (m), 1141 (s), 1130 (w), 1064 (s), 1021 (s), 915 (s, sh), 854 (m), 828 (s), 800 (m), 774 (s), 767 (s), 735 (s), 640 (m), 615 (m), 581 (m), 550 (m), 503 (s), 453 (s).

## Synthesis of $[\text{Cu}(\text{II})(\text{L}_4\text{H}_2)_2] \cdot 2\text{MeOH}$ (**2**)

$\text{Cu}(\text{NO}_3)_2 \cdot 3\text{H}_2\text{O}$  (0.025 g, 0.10 mmol), *N*-hydroxy-4-((2-hydroxybenzyl)amino)benzamide ( $\text{L}_4\text{H}_3$ ) (0.03 g, 0.11 mmol) and tetraethylammonium hydroxide (TEAOH) (0.015 g, 0.10 mmol) were dissolved in methanol (20 cm<sup>3</sup>) and stirred at room temperature for 3 h. The resultant yellowish green solution was then filtered and X-ray quality crystals of **2** were obtained upon slow evaporation of the mother liquor in 15% (9.1 mg; crystals) yield. Elemental analysis (%) calculated as **2** ( $\text{C}_{30}\text{H}_{34}\text{N}_4\text{O}_8\text{Cu}_1$ ): C 56.11, H 5.34, N 8.72; found: C 56.02, H 4.75, N 8.78. FT-IR (cm<sup>-1</sup>): 3624 (m), 3538 (s), 3391 (m), 3208 (w), 3132 (m), 3062 (w), 2940 (m), 2839 (w), 2723 (m), 2611 (m), 2233 (w), 2107 (w), 1899 (w), 1606 (s, sh), 1592 (s), 1533 (m), 1501 (s, sh), 1453 (s, sh), 1414 (w), 1395 (w), 1354 (w), 1333 (m), 1311 (w), 1273 (s), 1242 (s), 1195 (w), 1177 (s, sh), 1157 (w), 1110 (w), 1072 (s), 1033 (s, sh), 1013 (s), 920 (s, sh), 861 (w), 826 (s, sh), 762 (s, sh), 715 (m), 661 (s), 636 (s), 582 (s), 525 (w), 506 (s), 436 (s), 414 (s).

## Conflicts of interest

There are no conflicts to declare.

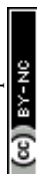
## Acknowledgements

BFM would like to thank the University of Maiduguri and the Petroleum Technology Development Fund (PTDF) for their award of an overseas fellowship. We would like to thank the EPSRC National Crystallographic Service at Southampton University for their continuous support. MPG would like to acknowledge support from KMITL (KREF046211). LFJ would like to thank the University of Wolverhampton for their support (JC).



## Notes and references

- 1 S. R. Batten, N. R. Champness, X.-M. Chen, J. Garcia-Martinez, S. Kitagawa, L. Öhrström, M. O'Keeffe, M. Paik Suh and J. Reedijk, *CrystEngComm*, 2012, **14**, 3002–3004.
- 2 (a) C.-T. Chen and K. S. Suslick, *Coord. Chem. Rev.*, 1993, **128**, 293–322; (b) C. Janiak, *Dalton Trans.*, 2003, 2781–2804; (c) S. Kitagawa and R. Matsuda, *Coord. Chem. Rev.*, 2007, **251**, 2490–2509; (d) J.-P. Zhang, Z.-C. Huang and X.-M. Chen, *Chem. Soc. Rev.*, 2009, **38**, 2385–2396; (e) C. Janiak and J. K. Vieth, *New J. Chem.*, 2010, **34**, 2366–2388; (f) W. L. Leong and J. J. Vittal, *Chem. Rev.*, 2011, **111**, 688–764.
- 3 (a) F. Thebault, S. A. Barnett, A. J. Blake, C. Wilson, N. E. Champness and M. Schröder, *Inorg. Chem.*, 2006, **45**, 6179–6187; (b) W. M. Bloch, C. J. Doonan and C. J. Sumby, *CrystEngComm*, 2013, **15**, 9663–9671; (c) M. Du, C.-P. Li, C.-S. Liu and S.-M. Fang, *Coord. Chem. Rev.*, 2013, **257**, 1282–1305.
- 4 (a) V. Niel, J. M. Martinez-Agudo, M. Carmen Muñoz, A. B. Gaspar and J. Antonio Real, *Inorg. Chem.*, 2001, **40**, 3838–3839; (b) G. J. Halder, C. J. Kepert, B. Moubaraki, K. S. Murray and J. D. Cashion, *Science*, 2002, **298**, 1762–1765; (c) S. M. Neville, G. J. Halder, K. W. Chapman, M. B. Duriska, B. Moubaraki, K. S. Murray and C. J. Kepert, *J. Am. Chem. Soc.*, 2009, **131**, 12106–12108; (d) W. Liu, X. Bao, L.-L. Mao, J. Tucek, R. Zboril, J.-L. Liu, F.-S. Guo, Z.-P. Ni and M.-L. Tong, *Chem. Commun.*, 2014, **50**, 4059–4061; (e) C. Bartual-Murgui, A. Akou, C. Thibault, G. Molnar, C. Vieu, L. Salmon and A. Bousseksou, *J. Mater. Chem. C*, 2015, **3**, 1277–1285; (f) Z.-P. Ni, J.-L. Liu, M. N. Hoque, W. Liu, J.-Y. Li, Y.-C. Chen and M.-L. Tong, *Coord. Chem. Rev.*, 2017, **335**, 28–43; (g) C. Pham and F. Paesani, *Inorg. Chem.*, 2018, **57**, 9839–9843; (h) A. Tissot, X. Keese, S. Giannopoulou, I. Stenger, L. Binet, E. Riviere and C. Serre, *Chem. Commun.*, 2019, **55**, 194–197.
- 5 (a) C. Coulon, H. Miyasaka and R. Clerac, *Struct. Bonding, Single-Molecule Magnets and Related Phenomena*, Springer, 2006, pp. 163–206; (b) L. Bogani, A. Vindigni, R. Sessoli and D. Gatteschi, *J. Mater. Chem.*, 2008, **18**, 4750–4758; (c) H.-L. Sun, Z.-M. Wang and S. Gao, *Coord. Chem. Rev.*, 2010, **254**, 1081–1100.
- 6 (a) A. D. Katsenis, E. K. Brechin and G. S. Papaefathiou, *Encyclopedia of Inorganic and Bioinorganic Chemistry*, Wiley Publishers, 2014, pp. 245–258; (b) J. J. Baldoví, E. Coronado, A. Gaita-Ariño, C. Gamer, M. Giménez-Marqués and G. Mínguez Espallargas, *Chem. – Eur. J.*, 2014, **20**, 10695–10702; (c) D. Aulakh, J. B. Pyser, X. Zhang, A. A. Yakovenko, K. R. Dunbar and M. Wreidt, *J. Am. Chem. Soc.*, 2015, **137**, 9254–9257; (d) X. Zhang, V. Vieru, X. Feng, J.-L. Liu, Z. Zhang, B. Na, W. Shi, B.-W. Wang, A. K. Powell, L. F. Chibotaru, S. Gao, P. Cheng and J. R. Long, *Angew. Chem., Int. Ed.*, 2015, **54**, 9861–9865; (e) C.-M. Liu, D.-Q. Zhang Hao and D.-B. Zhu, *Sci. Rep.*, 2017, **7**, 11156–11161.
- 7 (a) G. Givaja, P. Amo-Ochoa, C. J. Gómez-García and F. Zamora, *Chem. Soc. Rev.*, 2012, **41**, 115–147; (b) C. H. Hendon, D. Tiana and A. Walsh, *Phys. Chem. Chem. Phys.*, 2012, **14**, 13120–13132; (c) A. C. Talin, A. Centrone, A. C. Ford, M. E. Foster, V. Stavila, P. Haney, R. A. Kinney, V. Szalai, F. El Gabaly, H. P. Yoon, F. Léonard and M. D. Allendorf, *Science*, 2014, **343**, 66–69; (d) L. Sun, M. G. Campbell and M. Dinč, *Angew. Chem., Int. Ed.*, 2016, **55**, 3566–3579.
- 8 (a) L. Ma, O. R. Evans, B. M. Foxman and W. Lin, *Inorg. Chem.*, 1999, **38**, 5837–5840; (b) D. M. Ciurtun, N. G. Pschirer, M. D. Smith, U. H. F. Bunz and H.-C. zur Loye, *Chem. Mater.*, 2001, **13**(9), 2743–2745; (c) T. H. Kim, Y. W. Shin, J. H. Jung, J. S. Kim and J. Kim, *Angew. Chem., Int. Ed.*, 2008, **47**, 685–688; (d) Y. Hasegawa and T. Nakanishi, *RSC Adv.*, 2010, **5**, 338–353; (e) Y. Hasegawa, T. Nakanishi and Y. Kitagawa, *RSC Adv.*, 2018, 347–370; (f) W. P. Lustig and J. Lin, *Coord. Chem. Rev.*, 2018, **373**, 116–147.
- 9 (a) L. Ma, C. Abney and W. Lin, *Chem. Soc. Rev.*, 2009, **38**, 1248–1256; (b) J. Lee, O. K. Farha, J. Roberts, K. A. Scheidt, S. T. Nguyen and J. T. Hupp, *Chem. Soc. Rev.*, 2009, **38**, 1450–1459; (c) P. D. Tran, R. V. Tran, M. Orio, S. Torelli, Q. D. Truong, K. Nayuki, Y. Sasaki, S. Y. Chiam, R. Yi, I. Honma, J. Barber and V. Artero, *Nat. Mater.*, 2016, **15**, 640–646; (d) E. Loukopoulos and G. E. Kostakis, *J. Coord. Chem.*, 2018, **71**(3), 371–410.
- 10 (a) S. Kitagawa, R. Kitaura and S. Noro, *Angew. Chem., Int. Ed.*, 2004, **43**, 2334–2375; (b) M. L. Foo, R. Matsuda and S. Kitagawa, *Chem. Mater.*, 2014, **26**, 310–322.
- 11 (a) X. Lin, N. R. Champness and M. Schröder, *Top. Curr. Chem., Functional Metal-Organic Frameworks: Gas Storage, Separation and Catalysis*, Springer, 2010, vol. 293, pp. 35–76; (b) S. Ma and H.-C. Zhou, *Chem. Commun.*, 2010, **46**, 44–53; (c) B. Li, H.-M. Wen, W. Zhou and B. Chen, *J. Phys. Chem. Lett.*, 2014, **5**, 3468–3479; (d) J. Duan, W. Jin and R. Krishna, *Inorg. Chem.*, 2015, **54**, 4279–4284; (e) K. S. Song, D. Kim, K. Polychronopoulou and A. Coskun, *ACS Appl. Mater. Interfaces*, 2016, **8**, 26860–26867.
- 12 (a) P. Horcajada, C. Serre, M. Vallet-Regí, M. Sebban, F. Taulelle and G. Férey, *Angew. Chem., Int. Ed.*, 2006, **45**, 5974–5978; (b) P. Horcajada, T. Chalati, C. Serre, B. Gillet, C. Sebrie, T. Baati, J. E. Eubank, D. Hertaux, P. Clayette, C. Kreuz, J.-S. Chang, Y. K. Hwang, V. Marseaud, P.-N. Bories, L. Cynober, S. Gil, G. Férey, P. Couvreur and R. Gref, *Nat. Mater.*, 2010, **9**, 172–178; (c) R. C. Huxford, J. Della Rocca and W. Lin, *Curr. Opin. Chem. Biol.*, 2010, **14**, 262–268; (d) Z. Ma and B. Moulton, *Coord. Chem. Rev.*, 2011, **255**, 1623–1641; (e) I. Abánades Lázaro and R. S. Forgan, *Coord. Chem. Rev.*, 2019, **380**, 230–259.
- 13 (a) Z. Xie, L. Ma, K. E. deKrafft, A. Jin and W. Lin, *J. Am. Chem. Soc.*, 2010, **132**, 922–923; (b) H. Tan, B. Liu and Y. Chen, *ACS Nano*, 2012, **6**(12), 10505–10511; (c) X. Zhang, X. Luo, N. Zhang, J. Wu and Y.-Q. Huang, *Inorg. Chem. Front.*, 2017, **4**, 1888–1894; (d) C. Chen, X. Zhang, P. Gao and M. Hu, *J. Solid State Chem.*, 2018, **258**, 86–92; (e) M. Arici, *New J. Chem.*, 2019, **43**, 3690–3697.
- 14 C. McDonald, D. W. Williams, P. Comar, S. J. Coles, T. D. Keene, M. B. Pitak, E. K. Brechin and L. F. Jones, *Dalton Trans.*, 2015, **44**, 13359–13368.
- 15 A. F. Abdel-Magid, K. G. Carson, B. D. Harris, C. A. Maryanoff and R. D. Shah, *J. Org. Chem.*, 1996, **61**, 3849–3862.





- 16 M. B. Fugu, R. J. Ellaby, H. M. O'Connor, M. B. Pitak, W. Klooster, P. N. Horton, S. J. Coles, M. H. Al-mashhadani, I. F. Perepichka, E. K. Brechin and L. F. Jones, *Dalton Trans.*, 2019, **48**, 10180–10190.
- 17 (a) J. Yang, P. J. Bremer, I. L. Lamont and A. J. McQuillan, *Langmuir*, 2006, **22**, 10109–10117; (b) B. Kurzak, H. Kozlowski and E. Farkas, *Coord. Chem. Rev.*, 1992, **114**, 169–200.
- 18 (a) J. J. McKinnon, M. A. Spackman and A. S. Mitchell, *Acta Crystallogr., Sect. B: Struct. Sci.*, 2004, **60**, 627–668; (b) M. A. Spackman and D. Jayatilaka, *CrystEngComm*, 2009, **11**, 19–32; (c) S. L. Tan, M. M. Jotani and E. R. T. Tiekink, *Acta Crystallogr., Sect. E: Crystallogr. Commun.*, 2019, **75**, 308–318.
- 19 C. F. Matta, J. Hernández-Trujillo, T.-H. Tang and R. F. W. Bader, *Chem. – Eur. J.*, 2003, **9**, 1940–1951.
- 20 C. F. Macrae, I. J. Bruno, J. A. Chisholm, P. R. Edgington, P. McCabe, E. Pidcock, L. Rodriguez-Monge, R. Taylor, J. van de Streek and P. A. Wood, *J. Appl. Crystallogr.*, 2008, **41**, 466–470.
- 21 Rigaku OD, *CrysAlis PRO*, Rigaku Oxford Diffraction Ltd, Yarnton, England, 2015.
- 22 G. M. Sheldrick, Crystal structure refinement with SHELXL, *Acta Crystallogr., Sect. C: Struct. Chem.*, 2015, **71**, 3–8.
- 23 V. Dolomanov, L. J. Bourhis, R. J. Gildea, J. A. K. Howard and H. J. Puschmann, OLEX2: a complete structure solution, refinement and analysis program, *Appl. Crystallogr.*, 2009, **42**, 339–341.
- 24 M. J. Frisch, *Gaussian 16 Rev. C.01*, Wallingford, CT, 2016.
- 25 Y. Zhao and D. Truhlar, *Theor. Chem. Acc.*, 2008, **120**(1–3), 215–241.
- 26 D. Jayatilaka, S. K. Wolff, D. J. Grimwood, J. J. McKinnon and M. A. Spackman, *Acta Crystallogr., Sect. A: Found. Crystallogr.*, 2006, **62**, 90.

